J Mater Sci (2012) 47:7157–7166
DOI 10.1007/s10853-012-6656-z

In situ nitridation of titanium–molybdenum alloys during laser deposition

Tushar Borkar · Sundeep Gopagoni · Soumya Nag · J. Y. Hwang · Peter C. Collins · Rajarshi Banerjee

Received: 3 May 2012 / Accepted: 8 June 2012 / Published online: 22 June 2012

Abstract In situ nitridation during laser deposition of titanium–molybdenum alloys from elemental powder blends has been achieved by introducing the reactive nitrogen gas during the deposition process. Thus, Ti–Mo–N alloys have been deposited using the laser engineered net shaping (LENS^{TM}) process and resulted in the formation of a hard α(Ti,N) phase, exhibiting a dendritic morphology, distributed within a β(Ti–Mo) matrix with fine scale transformed α precipitates. Varying the composition of the $Ar + N_2$ gas employed during laser deposition permits a systematic increase in the nitrogen content of the as-deposited Ti–Mo–N alloy. Interestingly, the addition of nitrogen, which stabilizes the α phase in Ti, changes the solidification pathway and the consequent sequence of phase evolution in these alloys. The nitrogen-enriched hcp α(Ti,N) phase has higher c/a ratio, exhibits an equiaxed morphology, and tends to form in clusters separated by ribs of the Mo-rich β phase. The Ti–Mo–N alloys also exhibit a substantial enhancement in microhardness due to the formation of this α(Ti,N) phase, combining it with the desirable properties of the β-Ti matrix, such as excellent ductility, toughness, and formability.

T. Borkar · S. Gopagoni · S. Nag · P. C. Collins · R. Banerjee (✉)
Center for Advanced Research and Technology and Department of Materials Science and Engineering, University of North Texas, Denton, TX 76203, USA
e-mail: rajarshi.banerjee@unt.edu

J. Y. Hwang
Institute of Advanced Composite Materials, Korea Institute of Science and Technology, Jeonbuk 565-902, Korea

Introduction

Titanium alloys are attractive candidates for structural, marine, aerospace, biomedical (such as in dental and orthopedic as bone implants), and other industrial applications due to their excellent strength to weight ratio, ductility and formability, corrosion resistance and biocompatible properties. However, titanium alloys suffer from rather poor surface hardness and wear resistance properties. One way of improving the hardness as well as tribological properties of titanium alloys is by reinforcing the soft matrix with hard precipitates, such as titanium nitrides, carbides, and borides. These reinforcements can be introduced either via direct incorporation of such hard compounds in the matrix during processing [1, 2] or via in situ reaction with solid or gaseous precursors, resulting in the formation of hard precipitates [3–5], as well as via surface engineering techniques such as nitriding [6–8].

Focusing on nitride reinforced titanium alloys, the most commonly used technique is surface nitridation of these alloys via heating at elevated temperatures in a flowing nitrogen atmosphere [6–8]. Another approach that has been employed is the direct introduction of δ-TiN and TiB particles during laser deposition of Ti–6Al–4V [1, 2]. The forming processing approach, nitridation in a gaseous atmosphere, has been applied to the case of β Ti–Mo alloys, resulting in the formation of a continuous surface δ-TiN layer and a sub-surface microstructure consisting of laths (or plates) of either the same δ-TiN phase or a nitrogen-rich α(Ti,N) solid solution phase, dispersed within the β matrix [7, 8]. While such surface nitridation via heating in a nitrogen atmosphere is a simple and inexpensive way to achieve a case hardened layer, the time required and the depth of penetration are rather limited and it is difficult to introduce hard nitrides (or other

Table 1 Lattice parameters and d spacings of significant planes of alpha and beta phases in four different Ti–10Mo alloys

Alloy	d(011)β (Å)	d(10$\bar{1}$0)α (Å)	d(0002)α (Å)	aβ (Å)	aα (Å)	cα (Å)	c/a
Alloy 1 Ti–10Mo	2.304	2.553	2.347	3.258	2.948	4.694	1.59
Alloy 2 Ti–10Mo–25N_2	2.307	2.564	2.375	3.263	2.960	4.750	1.61
Alloy 3 Ti–10Mo–50N_2	2.305	2.564	2.382	3.260	2.960	4.764	1.61
Alloy 4 Ti–10Mo–75N_2	2.307	2.570	2.387	3.263	2.968	4.774	1.61

nitrogen-enriched hard phases) within the bulk of the material. The direct introduction of nitride and boride particles during laser deposition of titanium alloy powders can obviate this problem. However, the quality of such an interface between such externally introduced reinforcements and the alloy matrix can be rather difficult to control and, therefore, a reinforcement ideally created as a product of an in situ reaction offers the advantage of a thermodynamically stable and clean interface with the matrix. Furthermore, by employing an in situ nitride (or nitrogen-enriched hard α phase) formation reaction, a more uniform and homogeneous distribution of the nitride phase can be potentially achieved throughout the matrix.

The LENS^{TM} process, in recent years, is having a strong impact on the rapid prototyping, small-scale fabrication, and repair of complex parts in industry [9, 10]. Originally, the LENS^{TM} process was developed at Sandia National Laboratories and subsequently commercialized by Optomec Design Company. LENS^{TM} process uses focused laser beam for melting the metallic powders and 3D CAD files for designing the solid 3D object prior to fabrication [11]. In the present investigation, Ti–Mo alloys were deposited using the LENS^{TM} process under nitrogen atmosphere for the formation of in situ nitride or nitrogen-enriched hard phases. The focus is on developing a new class of Ti–Mo–N alloys with systematically controlled quantities of nitrogen and to investigate the microstructure and microhardness of this new class of alloys. The expectation is that the hard phases introduced will substantially improve the mechanical and tribological properties of the base Ti–Mo alloy. The novelty of this work primarily lies in the development of this new class of in situ nitride reinforced Ti–Mo–N alloys.

Experimental details

All the Ti–Mo and Ti–Mo–N alloys were deposited using commercial LENS^{TM} 750 system. LENS^{TM} process begins with CAD (computer aided design) file of 3D component, which is sliced into series of layers electronically. The information about each of these layers is transmitted to the manufacturing assembly. LENS system consists of mainly four parts: the laser system, the powder delivery system, the controlled environment glove box, and motion-controlled system. Powder feedstock is delivered through an inert gas flowing through multi-nozzle assembly into molten pool produced by focused high power laser to obtain homogeneity. The detailed mechanism of this process has been reported elsewhere [12, 13]. A titanium substrate is used as base for deposition of the component. The nozzles are designed in such a way so that powder feedstock converges at the same point into focused laser beam.

All depositions were carried out inside a glove box with controlled gas atmosphere. Pure Ar (Argon), 25 % N_2–75 % Ar, 50 % N_2–50 %Ar, and 75 % N_2–25 % Ar were the atmospheres used for fabrication of deposits. These alloys have been listed in Table 1 as Alloy 1 through Alloy 4, respectively. In addition, the powder carrier gas as well as the center purge gas, used in the LENS^{TM} system, were of the same composition. A high-powered 500 W Nd-YAG laser, emitting near-infrared laser radiation at a wavelength of 1.064 μm (1,064 nm) was focused on a titanium substrate to create a melt pool into which powder feedstock was delivered using Ar gas flowing through the multi-nozzle assembly. The powders used for deposition of Ti–Mo–N alloys are commercially available Ti and Mo powders. These powders in the ratio of Ti:Mo = 90:10, by weight, were mixed using twin-roller ball mill. The alloys were laser deposited in a cylindrical geometry of 10 mm diameter and height of 10 mm. The laser power used in these depositions was 350 W.

The LENS^{TM} deposited in situ alloys were characterized in FEI-Quanta Nova-SEM. X-ray diffraction analysis of deposits was performed using (1.54 CuKα) line of Rigaku Ultima III X-ray Diffractometer. The microhardness was measured using a standard vickers microhardness tester using 300 g load for 15 s. Average of 10 readings were taken into account. LENS^{TM} deposited alloys were also characterized by transmission electron microscopy (TEM). Site-specific TEM sample was made using Focused Ion

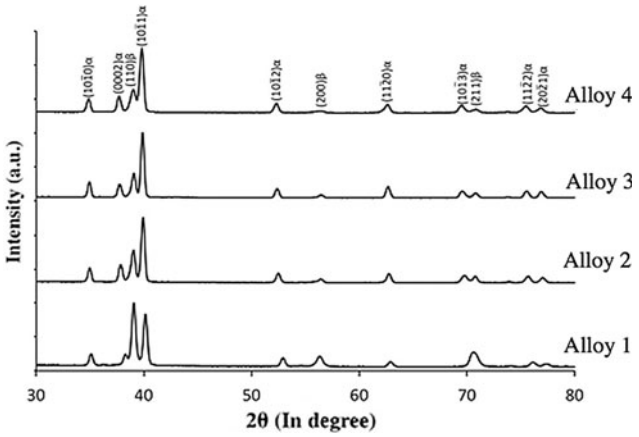

Fig. 1 XRD pattern obtained from LENS deposited Ti–Mo–N alloys (Alloy 1 to 4)

Beam (FIB). These TEM specimens were characterized in FEI Tecnai F20 FEG TEM operating at 200 keV.

Results and discussion

X-ray diffraction analysis

X-ray diffraction (XRD) patterns corresponding to the four as-deposited Ti–Mo–N alloys are shown in Fig. 1. The peaks in the diffraction patterns from all the four Ti–Mo–N alloys, with varying contents of N_2 used during the LENS^{TM} deposition can be consistently indexed based on the bcc β and hcp α phases. For convenience, the four Ti–Mo–N alloys will subsequently be referred to as Alloys 1, 2, 3, and 4, corresponding to the deposition conditions of 100 %Ar, 75 %Ar–25 %N_2, 50 %Ar–50 %N_2, and 25 % Ar–75 %N_2, respectively (Table 1). For the binary Ti–10Mo alloy, the (110)β peak exhibits the highest intensity qualitatively indicating that the β phase has the highest volume fraction in this alloy. Additionally, a substantial volume fraction of the α phase is also visible, as evident from the peaks in the diffraction pattern. As N_2 content in the alloy increases from alloy 1 to 4, there is a systematic decrease in intensity of the (011)β peak and a corresponding increase in the intensity of the $(10\bar{1}1)\alpha$ peak, which can be attributed to an increasing volume fraction of α in the Ti–Mo–N alloys. The ratio of peak intensities of $(10\bar{1}1)\alpha/(110)\beta$ as a function of N_2 content in the alloy, increases from 0.9 to 3.1, from alloy 1 to 4, respectively. The lattice parameters for both α and β phases have been analyzed in detail and the results have been summarized in Table 1. The lattice parameter of the β phase in case of all the alloys appears to be nearly constant and equals $\sim$3.26 Å. This value lies in between the β lattice parameters for elemental Ti ($\sim$3.3 Å) and Mo ($\sim$3.15 Å), suggesting that the β phase in these alloys is a Ti–Mo solid solution, which is expected considering that Mo is a strong β stabilizer in Ti alloys. In case of the α phase, both the "a" and "c" lattice constants appear to be increasing with increasing N_2 content in the alloy. However, the change in the value of c ($\sim$1.7 %) is larger as compared to the change in the value of a ($\sim$0.67 %), indicating a change in the c/a ratio for the hcp α phase. While the c/a for alloy 1 equals 1.59 and is almost identical to the value for the α phase in elemental Ti, the c/a value for all the nitrogen-containing alloys is larger and equals 1.61. The higher c/a value is a clear indication of the incorporation of nitrogen into the hcp α phase of Ti, and the experimentally measured value of 1.61 in these alloys is identical to the value reported for the $TiN_{0.3}$ phase based on the ICCD database as well as other references [6]. Thus, it can be concluded that the α phase in case of the nitrogen-containing Ti–Mo–N alloys (Alloys 2, 3, and 4), is a nitrogen-enriched α(Ti,N) hcp phase (Space group $P6_3/mmc$) wherein the nitrogen atoms are expected to randomly occupy octahedral interstitial sites within the hcp lattice [6]. The same phase has also been referred to as α-$TiN_{0.3}$ in the International Center for Diffraction Data (ICDD) files obtained from Joint Committee of Powder Diffraction Standards (JCPDS). However, to prevent any confusion between the ordered titanium nitride phase (typically referred to as δ-TiN) and the random solid solution of nitrogen in α-Ti, the latter phase will be subsequently referred to as α(Ti,N).

Scanning electron microscopy analysis

A series of backscattered SEM images recorded from the Ti–Mo–N alloys are shown in Fig. 2 and 3. Figure 2a, b show the microstructure for the binary Ti–Mo alloy deposited in 100 % Ar atmosphere. The nominal composition of this alloy measured using EDS in the SEM is Ti–10 wt%Mo. The microstructure primarily consists of uniformly distributed fine scale precipitates of a second phase, presumably α precipitates, exhibiting a bimodal size distribution within the β-matrix. This bimodal size distribution of α precipitates can be rationalized on the basis of a two-step decomposition of the β-matrix, wherein the coarser α precipitates presumably result from the deposition of the layer during LENS^{TM} processing, while solid-state re-heating of the same layer, when the subsequent layer is being deposited on the top, results in the secondary decomposition of β forming the finer scale α. The inherent rapid cooling rates involved in laser deposition, also contribute to such non-equilibrium β decomposition processes. Thus, during laser deposition of a layer, the phase evolution follows the sequence liquid to β to $\beta + \alpha$, the inherently rapid cooling rates involved do not result in an equilibrium composition of the β matrix. Therefore, on

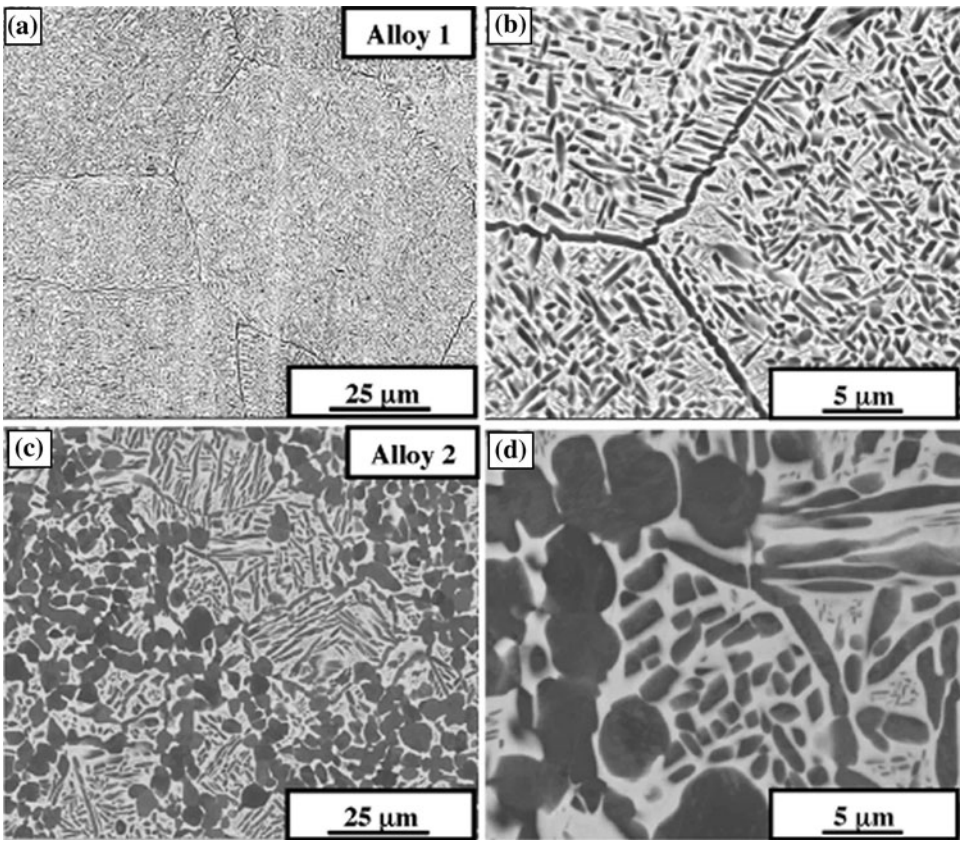

Fig. 2 **a** Low and **b** high magnification backscatter SEM image of LENS deposited Alloy 1. **c** Low and **d** high magnification backscatter SEM image of LENS deposited Alloy 2

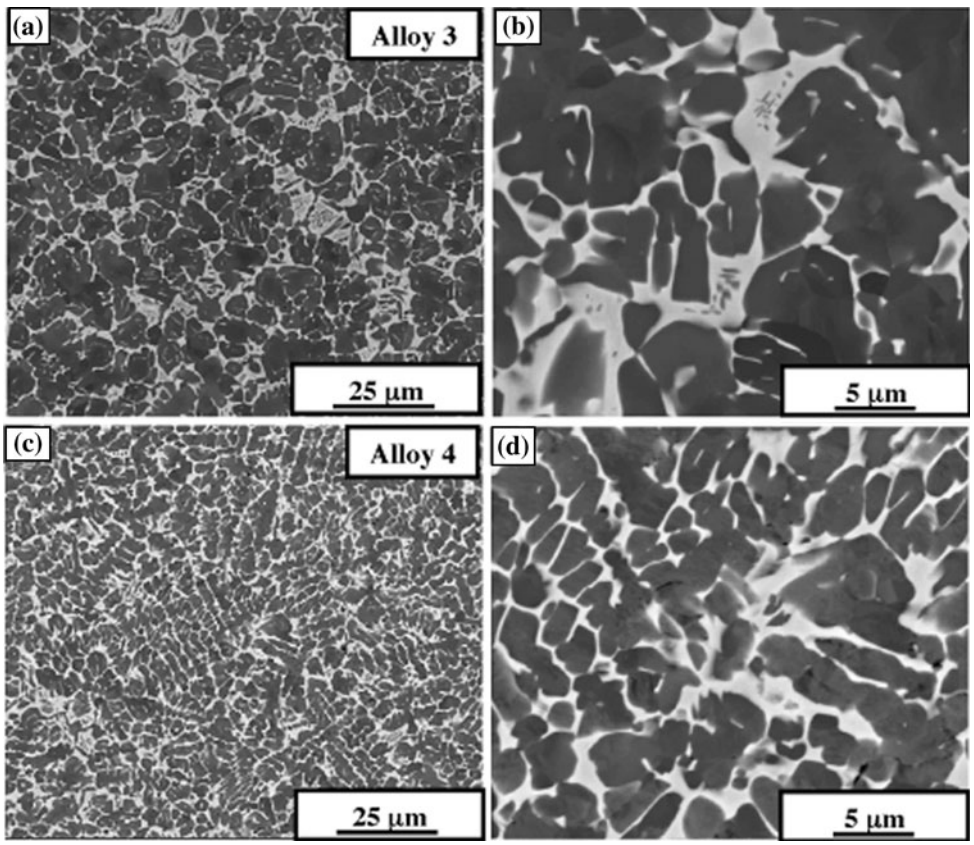

Fig. 3 **a** Low and **b** high magnification backscatter SEM image of LENS deposited Alloy 3. **c** Low and **d** high magnification backscatter SEM image of LENS deposited Alloy 4

subsequent re-heating of the same layer when a layer on top is being deposited, there is a further decomposition of the retained β matrix to form fine scale secondary α precipitates. The aspect ratio of this finer scale α is substantially larger than those of the coarser α precipitates.

Figure 2c and d show the microstructure of the Ti–Mo–N alloy deposited using a 75 % Ar–25 % N_2 atmosphere in the LENS^{TM} glovebox as well as the center gas purge and the powder carrier gas. The microstructure clearly exhibits two precipitate phases with rather different morphologies. The coarser precipitates appear to exhibit an equiaxed or globular morphology with curved interfaces separating them from the β matrix, suggesting that these interfaces are presumably incoherent in nature. In contrast, the finer scale precipitates exhibit a more sharper faceted morphology suggesting that the precipitate/matrix interface is likely to be semi-coherent. The identity of these two types of precipitates cannot be determined based solely on the backscatter SEM evidence presented in Fig. 2c and d. However, the morphology and contrast of the finer scale precipitates suggests that these α precipitates exhibited smaller aspect ratios as compared with those observed in case of the binary Ti–10Mo alloy deposited under a pure Ar atmosphere (Fig. 2a, b). As the N_2 content in the Ar + N_2 mixture used in LENS^{TM} deposition increases, the size and volume fraction of the coarser equiaxed second phase precipitates increases significantly in the microstructure, as revealed in Fig. 3a–d. Figure 3a and b correspond to Ti–10Mo alloys LENS^{TM} deposited under a 50 % Ar–50 %N_2 mixture while Fig. 3c and d correspond to an alloy deposited under a 25 % Ar–75 % N_2 mixture. There is also a corresponding decrease in the β volume fraction with increasing N_2 content in the gaseous atmosphere used for deposition. Thus, the primary microstructural influence of introducing nitrogen during laser deposition appears to be the formation of a novel equiaxed precipitates within the β matrix together with finer scale α precipitates, with the volume fraction of the equiaxed precipitates increasing with increasing nitrogen content in the alloy. However, it should be noted that the XRD results from all these alloys (Fig. 1) exhibited only two distinct phases, α(Ti,N) and β. There is no substantial volume fraction of a third phase in these XRD patterns. Therefore, the equiaxed precipitates appearing in the microstructure of alloys 2, 3, and 4, have to correspond to the α(Ti,N) phase. This has been further validated via detailed TEM investigations carried out on one of the Ti–Mo–N alloys, i.e., alloy 4, containing the maximum amount of N_2.

Transmission electron microscopy and orientation imaging microscopy analysis

Site-specific TEM samples have been extracted from alloy 4 using dual-beam focused ion beam instrument (FIB). The specific regions identified for this extraction included both the primary dendritic phase as well as the more refined and faceted α precipitates within the β matrix. A lower magnification scanning transmission electron microscopy (STEM) image of the entire site-specific sample, acquired using a high-angle annular dark-field (HAADF) detector, is shown in Fig. 4a. Three main areas were primarily analyzed—the equiaxed α regions, intragranular α precipitates, and the grain boundary α lying within the β-matrix. While in the SEM microstructure, the equiaxed region, from which the TEM foil was extracted, appeared to be a single coarse precipitate, as evident from the TEM micrograph in Fig. 4a, the same region appears to consist of an aggregate of multiple precipitates. Figure 4b and c show bright-field and dark-field images of one of the precipitates within this aggregate. Selected area diffraction (SAD) patterns from this region, such as the one shown as an inset in Fig. 4c, can be consistently indexed based on the hcp α phase with a c/a ratio of 1.61. This result clearly validates that the coarse equiaxed phase in the nitrogen containing Ti–Mo–N alloys, is the hcp α(Ti,N) phase, consistent with the macroscopic phase identification based on XRD results. Additionally, these precipitates also exhibit faults as shown in Fig. 4b and c. Such a high density of faults is characteristic of the hcp α(Ti,N) phase, also referred to as α-$TiN_{0.3}$, as reported previously [14]. As N atoms occupy the octahedral interstitial site of α-structure (Ti), it increases the packing density consequently decreasing the stacking fault energy. These faults typically lie on the (0001) basal planes of α, since the nitrogen atoms going into octahedral interstitial sites i.e., between the basal planes, increases the c/a ratio [6]. Bright- and dark-field TEM images of one of the intragranular α precipitates along with the corresponding SAD pattern are shown in Fig. 4d and e. The SAD pattern from this intra-granular precipitate (shown as an inset in Fig. 4e) can be consistently indexed as the [01-11] zone axis of α-Ti.

The aggregates or clusters of α(Ti,N) precipitates are more clearly visible in the higher magnification HAADF-STEM image shown in Fig. 5. The contrast within this HAADF image shows that the individual precipitates within this cluster are separated by thin layers exhibiting a very bright contrast, suggesting that these layers are rich in Mo. Thus, these inter-precipitate layers are likely to be very thin layers of β separating the equiaxed α(Ti,N) precipitates within a cluster or aggregate. Further detailed analysis of these equiaxed precipitates within a cluster has been carried out by orientation imaging microscopy (OIM^{TM}) studies using an electron backscatter diffraction (EBSD) detector in an SEM, the results of which are presented in Figs. 6 and 7. Figure 6a shows a backscatter SEM image of the exact same region in alloy 4 where the OIM^{TM}-EBSD scan was carried out. Figure 6b shows the

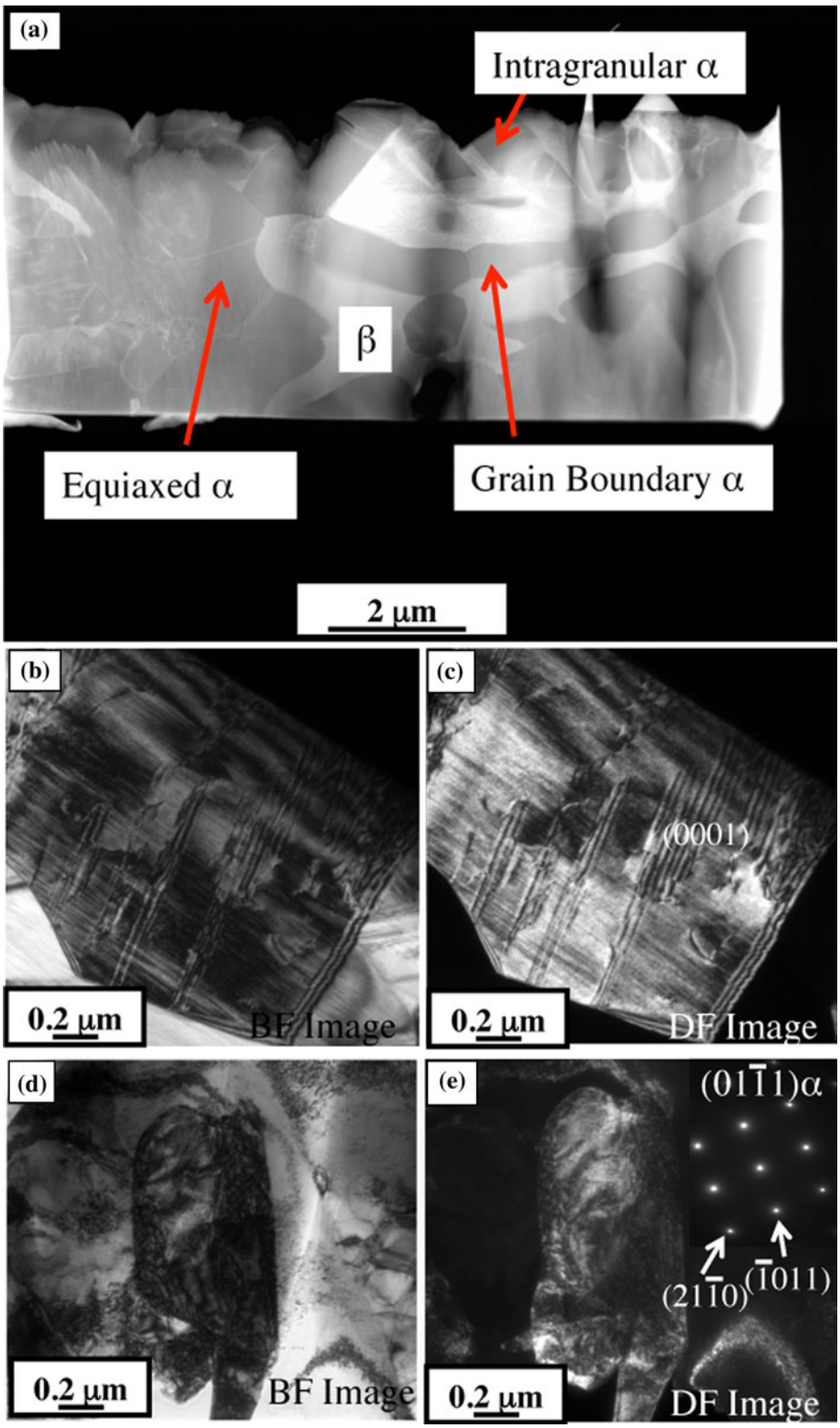

Fig. 4 **a** Scanning transmission electron microscopy (STEM) image of a site-specific sample made from Alloy 4, acquired using a high-angle annular dark-field (HAADF) detector. **b** Bright-field and **c** dark-field TEM images of one of the precipitates within the aggregate that form equiaxed α. **d** Bright-field and **e** dark-field TEM images of one of the intragranular α precipitates

pseudo-colored OIM^{TM} map of this region wherein both α(Ti,N) and β phases have been attributed colors based on their respective Euler angles. A more detailed analysis of the α(Ti,N) precipitates within two specific equiaxed α clusters and also an intra-granular secondary α precipitate, are shown in Fig. 7. The pseudo-colored OIM^{TM} map of the first cluster and corresponding α and β pole figures are shown in Fig. 7a. The region corresponding to this cluster has been marked in the overall OIM^{TM} map (Fig. 6b) as well as in the backscatter SEM image (Fig. 6a). The cluster

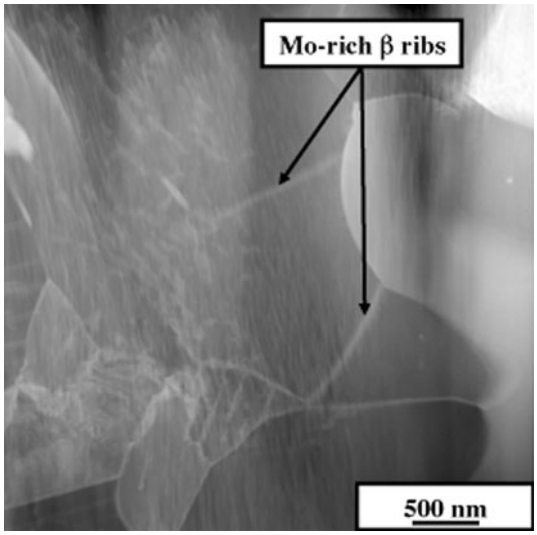

Fig. 5 High magnification HAADF-STEM image showing a cluster of α(Ti,N) precipitates

shown in Fig. 7a comprises six distinctly oriented α precipitates, marked 1–6 on the OIM^{TM} map and their corresponding (0001)α poles have been marked on the pole figure. In addition, the $\{11\bar{2}0\}\alpha$ poles for these precipitates as well as $\{011\}\beta$ and $\{111\}\beta$ pole figures for the surrounding β grain are shown in Fig. 7a. It is rather interesting to note that four of the six (0001)α poles (1,2,3,4) lie close to corresponding $\{011\}\beta$ poles but not exactly on these poles. Interestingly, further analysis of the EBSD-OIM^{TM} dataset revealed that the measured misorientation angles between two adjacent α precipitates shown in Fig. 7a, corresponds to a rotation ~70° about the common $\{11\bar{2}0\}$ pole between these two precipitates. Furthermore, this common $\{11\bar{2}0\}$ pole between two adjacent precipitates lies close to one of the $\{111\}\beta$ poles of the surrounding grains, but again not exactly parallel to it. All these observations clearly indicate a near-Burgers orientation relationship (i.e., $(0001)\alpha//\{011\}\beta$ and $\langle 11\bar{2}0\rangle\alpha//\langle 111\rangle\beta$) between all the α precipitates within a cluster and the surrounding the β grain. However, there is a clear departure from the exact Burgers relationship. The α precipitate, marked as 5 in this cluster, does not appear to have even a near-Burgers orientation relationship with the surrounding β grain. An identical scenario develops in case of the second cluster shown in Fig. 7b, the corresponding regions have been marked in Fig. 6a and b. In this case, five distinct α orientations are observed in the cluster and have been marked as 1–5

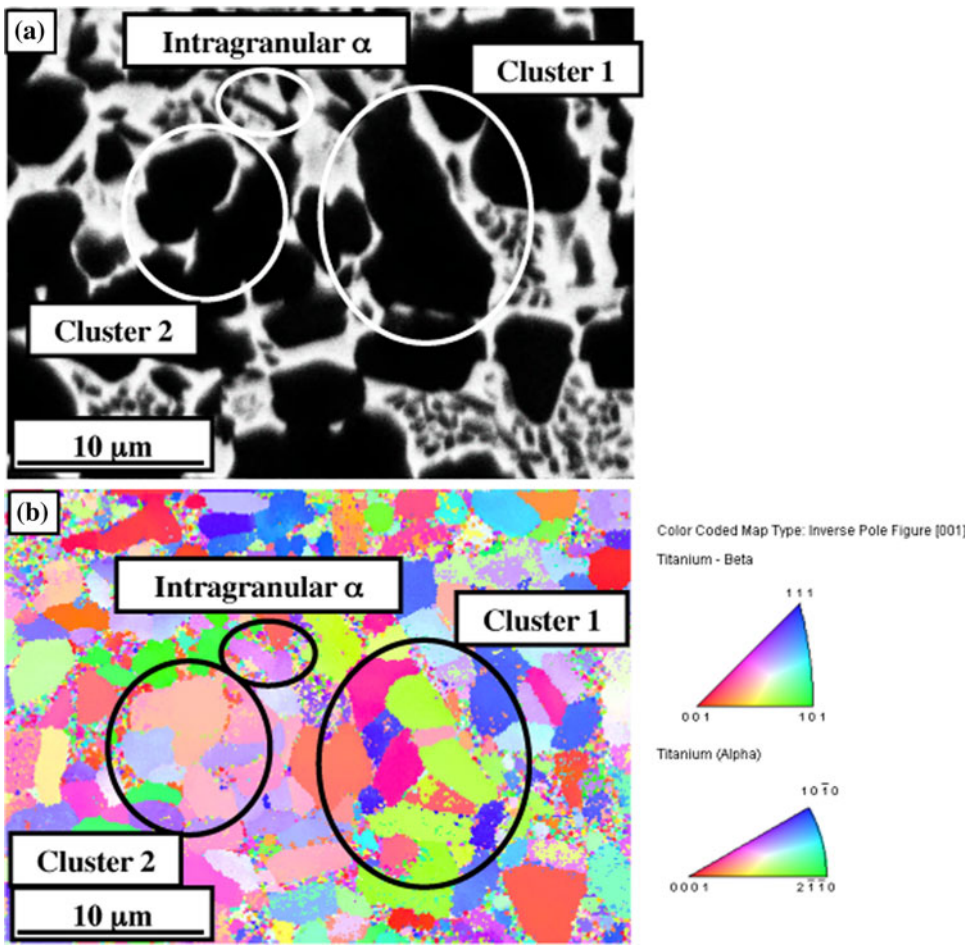

Fig. 6 **a** Backscatter SEM image and **b** corresponding pseudo-colored OIM^{TM} map of a region in alloy 4 where the EBSD scan was carried out. On both the images, two specific equiaxed α clusters and also an intra-granular secondary α precipitate has been *marked*

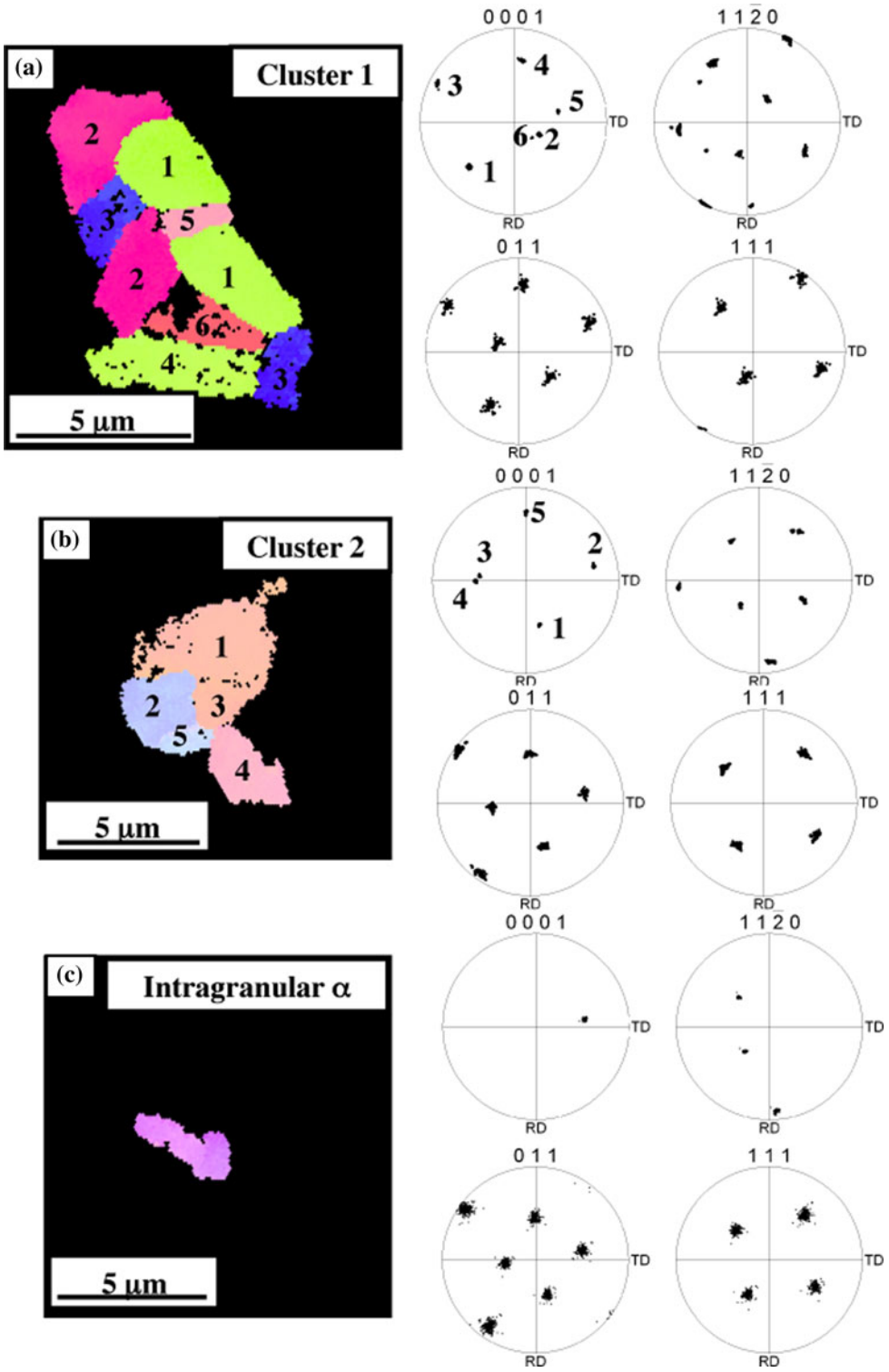

Fig. 7 Pseudo-colored OIM^{TM} map and corresponding α and β pole figures of **a** cluster 1, **b** cluster 2, and **c** intragranular α

both in the OIM^{TM} map as well as in the $(0001)\alpha$ pole figure. As in case of the first cluster, the misorientation between adjacent α precipitates in this cluster, i.e., 1,2,5,4 is also $\sim 70°$, about the common $\{11\bar{2}0\}$ pole between these two precipitates. These observations clearly suggest that these equiaxed α precipitates constituting a cluster, nucleated within the same β grain and presumably exhibited the energetically favorable Burgers orientation relationship at their nucleation stage. However, as these α precipitates grew and coarsened, the high misfit between the α(Ti,N) phase (with a larger c/a = 1.61 as compared to α-Ti) and the surrounding β matrix, led to a rapid increase in strain energy and a loss of semi-coherency at the

interface leading to the formation of incoherent α/β interfaces that subsequently developed a curved nature and also resulted in the equiaxed morphology of these precipitates. The high Mo content of the β matrix also plays a significant role in enhancing the misfit between these two phases, since the β-Ti lattice parameter is substantially reduced on alloying with Mo.

Finally, EBSD-OIM^{TM} analysis of an intra-granular α precipitate, exhibiting a more faceted lath or plate-like morphology is shown in Fig. 7c. The $(0001)\alpha$ and $\{11\bar{2}0\}\alpha$ pole figures for this precipitate as well as $\{011\}\beta$ and $\{111\}\beta$ pole figures for the surrounding β grain are also shown. An exact Burgers orientation relationship of the type $(0001)\alpha//\{011\}\beta$ and $\langle 11\bar{2}0\rangle\alpha//\langle 111\rangle\beta$ is evident between this α precipitate and the surrounding the β grain. This and other similar observations confirm that the intra-granular fine scale secondary α precipitates exhibit the typical lath or plate-like morphology and have a Burgers orientation relationship with the β matrix.

Evolution of microstructure in laser-deposited Ti–Mo–N alloys

Based on the experimental results from the various techniques discussed previously, an overall sequence of microstructural evolution in the Ti–Mo–N alloys can be developed. Thus, during the initial stages of a layer being deposited (via LENS^{TM} processing), there is a solidification of a mixture of titanium and molybdenum powders fed into a molten pool in an atmosphere enriched in nitrogen. The nitrogen dissolves in this localized Ti–Mo melt pool and the liquid solidifies. During solidification, the entire liquid transforms to the β phase which is supersaturated with nitrogen at high temperatures. During the cooling of the β phase in the solid state, precipitation of the α phase is initiated below the β transus temperature for this ternary Ti–Mo–N composition. Nitrogen, being a strong α stabilizer, naturally partitions strongly to the precipitating α phase forming the α(Ti,N) phase. The Mo, in contrast, is a strong β stabilizer and hence partitions to the β matrix. As precipitates of α(Ti,N) grow within the β matrix, both during cooling as well as solid-state re-heating of the same layer during subsequent depositions of layers on top, the strain energy increases rather rapidly due to the large misfit between the nitrogen-rich α(Ti,N) phase and the Mo-rich surrounding β matrix. This leads to the loss of coherency at the α(Ti,N)/β-Ti(Mo) interface, resulting in the formation of curved interfaces, as well as a more equiaxed morphology of these precipitates. Furthermore, there is a departure from the Burgers orientation relationship between the α(Ti,N) precipitates and the surrounding β matrix as these precipitates grow and coarsen. Additionally, it should be noted that the Mo-rich β matrix does not achieve equilibrium during the deposition of the layer. Therefore, the subsequent solid-state re-heating of the same layer also results in the precipitation of finer scale secondary α within the β matrix. Presumably, this finer scale secondary α contains a substantially lower amount of nitrogen as compared with the primary α(Ti,N) phase. While this has not been experimentally proven, it can be speculated based on the fact that during the precipitation of the primary α(Ti,N) phase, most of the nitrogen partitions to this phase with only a negligible amount retained in the β matrix. Consequently, the secondary α precipitates exhibit a lower misfit with the β matrix, thus retaining an exact Burgers orientation relationship, as well as a more typical lath or plate-like morphology with faceted interfaces.

Vickers microhardness results

The Vickers microhardness values for all the four alloys, 1 to 4, have been plotted in Fig. 8. A systematic increase in the microhardness values, with increasing nitrogen content in the alloys can be clearly observed. The binary Ti–Mo alloy, LENS^{TM} deposited under a pure Ar atmosphere, exhibits an average hardness of $\sim$500 HV. The increase in microhardness of the Ti–Mo–N alloys, with increasing N_2 content in the reactive atmosphere during LENS^{TM} deposition, can be attributed to the formation of the α-$TiN_{0.3}$ random solid solution hcp phase. For the highest nitrogen-containing alloy 4, the microhardness value is $\sim$800 HV, which is $\sim$60 % higher as compared with the LENS^{TM} deposited binary Ti–10 wt%Mo (alloy 1).

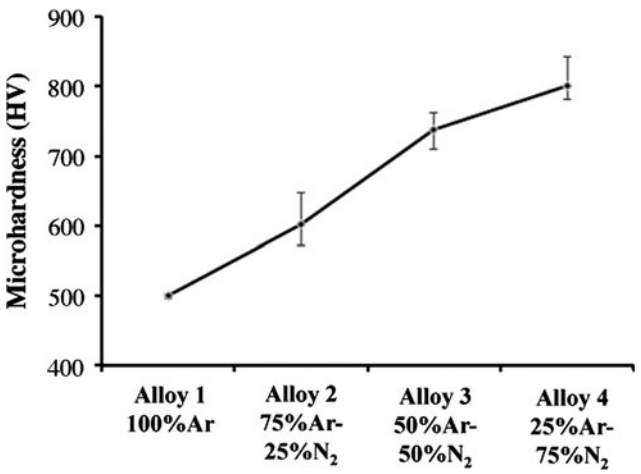

Fig. 8 A plot showing the variation in Vickers microhardness values for LENS deposited Ti–Mo–N alloys (Alloy 1 to 4)

Summary and conclusions

In situ nitridation of Ti–10 wt%Mo alloys has been achieved by the introduction of reactive nitrogen gas during the laser deposition (LENS^{TM}) of these alloys from elemental powder blends. The nitrogen content in these laser-deposited alloys has been tuned via changing the ratio of argon to nitrogen used in LENS^{TM} deposition. The enrichment of these alloys with nitrogen results in the formation of primary precipitates of the α(Ti,N) phase within the β matrix. The higher c/a ratio of these hcp α(Ti,N) precipitates, coupled with the Mo enrichment in the β matrix, results in a substantially large misfit, consequently leading to a loss of precipitate/matrix coherency during growth and coarsening. This results in the α(Ti,N) precipitates adopting an equiaxed morphology, and they tend to aggregate into clusters separated by thin Mo-rich β ribs. These α(Ti,N) precipitates increase the microhardness of the alloy to a substantial degree. Additional fine scale secondary α precipitates, exhibiting a lath or plate-like morphology, are also formed within the retained β matrix of these Ti–Mo–N alloys. The ability to introduce controlled volume fractions of the hard nitrogen-enriched α(Ti,N) phase can be very useful in tailoring the local microhardness and consequently wear resistance of these alloys. Furthermore, using the LENS^{TM} process it is possible to grade the nitrogen content within the same alloy and thus process a compositionally graded microstructure with systematically varying properties.

Acknowledgements This work has been supported by the ISES contract awarded to the University of North Texas by the US Air Force Research Laboratory, AFRL contract number FA8650-08-C-5226, with Dr. Jay Tiley as the program manager. The authors also gratefully acknowledge the Center for Advanced Research and Technology (CART) at the University of North Texas.

References

1. Balla V, Bhat A, Bose S, Bandopadhyay A (2012) J Mech Behav Biomed Mater 6:9
2. Das M, Balla V, Basu D, Manna I, Kumar T, Bandopadhyay A (2012) Scripta Mater 66:578
3. Banerjee R, Collins P, Fraser H (2002) Adv Eng Mater 4:847
4. Samual S, Nag S, Scharf T, Banerjee R (2008) Mater Sci Eng C 28:414
5. Nag S, Samual S, Puthucode A, Banerjee R (2009) Mater Charact 60:106
6. Bars J, David D, Etchessahar E, Debuigne J (1983) Metall Trans 14A:1537
7. Gordin D, Thibon I, Guillou A, Cornen M, Gloriant T (2010) Mater Charact 61:376
8. Gordin D, Guillou A, Thibon I, Bohn B, Ansel D, Gloriant T (2008) J Alloy Compd 457:384
9. Banerjee R, Collins P, Fraser H (2002) Metall Mater Trans A 33A:2129
10. Collins P, Banerjee R, Banerjee S, Fraser H (2003) Mater Sci Eng A A352:118
11. Gopagoni S, Hwang J, Singh A, Mensah B, Brunce N, Tiley J, Scharf T, Banerjee R (2011) J Alloy Compd 509:1255
12. Scharf T, Neira A, Hwang J, Tiley J, Banerjee R (2009) J Appl Phys 106:1
13. Wu X, Mei J (2003) J Mater Process Technol 135:266
14. Sundgren J (1985) Thin Solid Films 128:21